Slow build-up of turbidity currents triggered by a moderate earthquake in the Sea of Marmara

Pierre Henry[1], M Sinan Özeren[2], Nurettin Yakupoğlu[3], Ziyadin Çakir[3], Emmanuel de Saint-Léger[4], Olivier Desprez de Gésincourt[4], Anders Tengberg[5], Cristele Chevalier[6], Christos Papoutsellis[1], Nazmi Postacıoğlu[7], Uğur Dogan[8], Hayrullah Karabulut[9], Gülsen Uçarkuş[3], M Namık Çağatay[3]

[1]Aix Marseille Univ, CNRS, IRD, INRAE, Coll France, CEREGE, Aix-en-Provence, France, [2]Istanbul Technical University, Eurasia Institute of Earth Sciences, Maslak, Istanbul, Turkey, [3]Istanbul Technical University, Geological Engineering Dept., Maslak, Istanbul, Turkey, [4]CNRS, DT INSU, Parc national d'instrumentation océanographique, Plouzané, France, [5]Aanderaa Data Instruments AS, Bergen, Norway, [6]Aix Marseille Univ, CNRS, IRD, MIO, Aix-en-Provence, France, [7]Istanbul Technical University, Physics Dept., Maslak, Istanbul, Turkey, [8]Yıldız Technical University, Geomatic Engineering Dept., Istanbul, Turkey, [9]Bogazici University, KOERI, Istanbul, Turkey

Correspondence to: Pierre Henry (henry@cerege.fr)

Abstract. Earthquake-induced submarine slope destabilization is known to cause debris flows and turbidity currents, but the hydrodynamic processes associated with these events remain poorly understood. Records are scarce and this notably limits our ability to interpret marine paleoseismological sedimentary records. An instrumented frame comprising a pressure recorder and a Doppler recording current meter deployed at the seafloor in the Sea of Marmara Central Basin recorded consequences of a $M_W = 5.8$ earthquake occurring Sept 26, 2019 and of a $M_w = 4.7$ foreshock two days before. The smaller event caused sediment resuspension but no strong current. The larger event triggered a complex response involving a mud flow and turbidity currents with variable velocities and orientations, which may result from multiple slope failures. A long delay of 10 hours is observed between the earthquake and the passing of the strongest turbidity current. The distance travelled by the sediment particles during the event is estimated to several kilometres, which could

account for a local deposit on a sediment fan at the outlet of a canyon, but not for the covering of the whole basin floor. We show that after a moderate earthquake, delayed turbidity current initiation may occur, possibly by ignition of a cloud of resuspended sediment. Some caution is thus required when tying seismoturbidites with earthquakes of historical importance. However, the horizontal extent of the deposits should remain indicative of the size of the earthquake.

1. Introduction

Triggering of mass flows and turbidity currents by earthquakes is a hazard that can damage infrastructure at the seafloor (Heezen et al., 1954) and may enhance co-seismic tsunami generation (Okal and Synolakis, 2001; Synolakis et al., 2002; Hebert et al., 2005; Ozeren et al., 2010). It is often considered that a peak ground acceleration (PGA) of the order of 0.1 g is needed for an earthquake to trigger a submarine slope instability (Dan et al., 2008; Nakajima and Kanai, 2000). However, a global compilation of cable breaks shows that, exceptionally, mass flow have been triggered by individual earthquakes of M_w as low as 3.1 (with PGA $\approx 10^{-3}$ g) and that, on the other hand many M_w>7 have failed to break cables, notably in zones (e.g. Japan Trench) where sediment input is relatively low and earthquakes frequent (Pope et al., 2016). In the Mediterranean region, the threshold is reportedly around M_w = 5.

In spite of this high regional variability, turbidite deposits in several seismically active zones have been used successfully as paleoseimological event markers (Goldfinger et al., 2003, 2012; McHugh et al., 2014; Ikehara et al., 2016). This requires distinguishing between seismoturbidites, caused by earthquakes and related mass wasting events, from those resulting from other processes (e.g. floods, storms, sediment loading). Seismoturbidites are generally described as turbidite-homogenites where a basal silt-sand bearing layer is overlaid by a layer of apparently homogenous mud with small or gradual, if any, variations in grain size and chemical composition (Polonia et al., 2013; McHugh et al., 2011; Çağatay et al. 2012; Eriş et al., 2012; Gutierrez-Pastor et al., 2013; Beck et al., 2007). In lakes and closed basins several characteristics of deposits following earthquake or landslides, such as the sharp boundary between turbidite and homogenite layers, the alternation of silt/sand and mud laminae within a single turbidite-homogenite unit and presence of bi-directional cross- or flaser- bedding have been interpreted as indicators of deposition from oscillatory currents associated with seiches or turbidity current reflection (Beck et al.,

2007; Çağatay et al. 2012; McHugh et al., 2011). Seismoturbidites on ocean margins have fairly similar characteristics to those in closed basins but their layering has been interpreted differently, as a consequence of confluence (stacked or amalgamated turbidites) or current speed variations (multi-pulsed turbidites) (Gutierrez-Pastor et al., 2013; Nakajima and Kanai, 2000; Goldfinger et al., 2003). There is currently a lack of in situ records that could substantiate inferred hydrodynamic processes. Monitoring experiments brought records of representative cases of turbidity currents flowing in submarine canyons and initiated by meteorological events and occasionally by landslides (Azpiroz-Zabala et al., 2017; Khripounoff et al., 2012; Xu et al., 2004, 2010; Liu et al., 2012; Hughes Clarke, 2016). Oscillatory currents resulting from internal waves have been recorded after landslides in lakes (Brizuela et al., 2019). On the other hand, most information on earthquake-triggered events is still indirect based on cable ruptures (e.g. Pope, 2017; Hsu et al., 2008), combined with geomorphological and sedimentological observations (Cattaneo et al., 2012; Piper et al., 1999), and information from displaced instruments (Garfield et al., 1994). In Japan, in situ records of pressure and temperature were obtained from displaced OBSs after the Tohoku 2011 M_w 9.1 earthquake (Arai et., 2013), and from cabled observatories after the Tokachi-Oki 2003 M_w 8.3 earthquake (Mikada et al., 2006) and after a moderate (M 5.4) earthquake off Izu Penninsula (Kasaya et al., 2009). After the large events, strong currents of more than 1 m/s were implied starting 2-3 hours after the earthquake with no indication of oscillation or pulsing. In the off-Izu case a mudflow was observed with a camera 5 minutes after the earthquake and followed 15 minutes later by a change in current direction and speed.

We here present results from an instrumental deployment at the seafloor that accidentally recorded the consequences of earthquakes that occurred 09/24/2019 and 09/26/2019 in the Sea of Marmara with respective magnitudes 4.7 and 5.8 (Figure 1A). Holocene seismoturbidite records in the Sea of Marmara basins display a recurrence of 200 to 300 years, that roughly corresponds to the recurrence interval of Mw>7 earthquakes (McHugh et al., 2006, 2014; Drab et al., 2012, 2015; Yakupoğlu et al., 2018; Bulut et al., 2019). The pressure, temperature and current record from this single instrument demonstrate that this moderate earthquake triggered turbidity currents. However, the instrument suffered a rather complex sequence of disturbances and a 10 hours delay is observed between the earthquake and the recording of peak current.

We here propose a scenario which could explain the observations and discuss their implications for the understanding of seismoturbidite records.

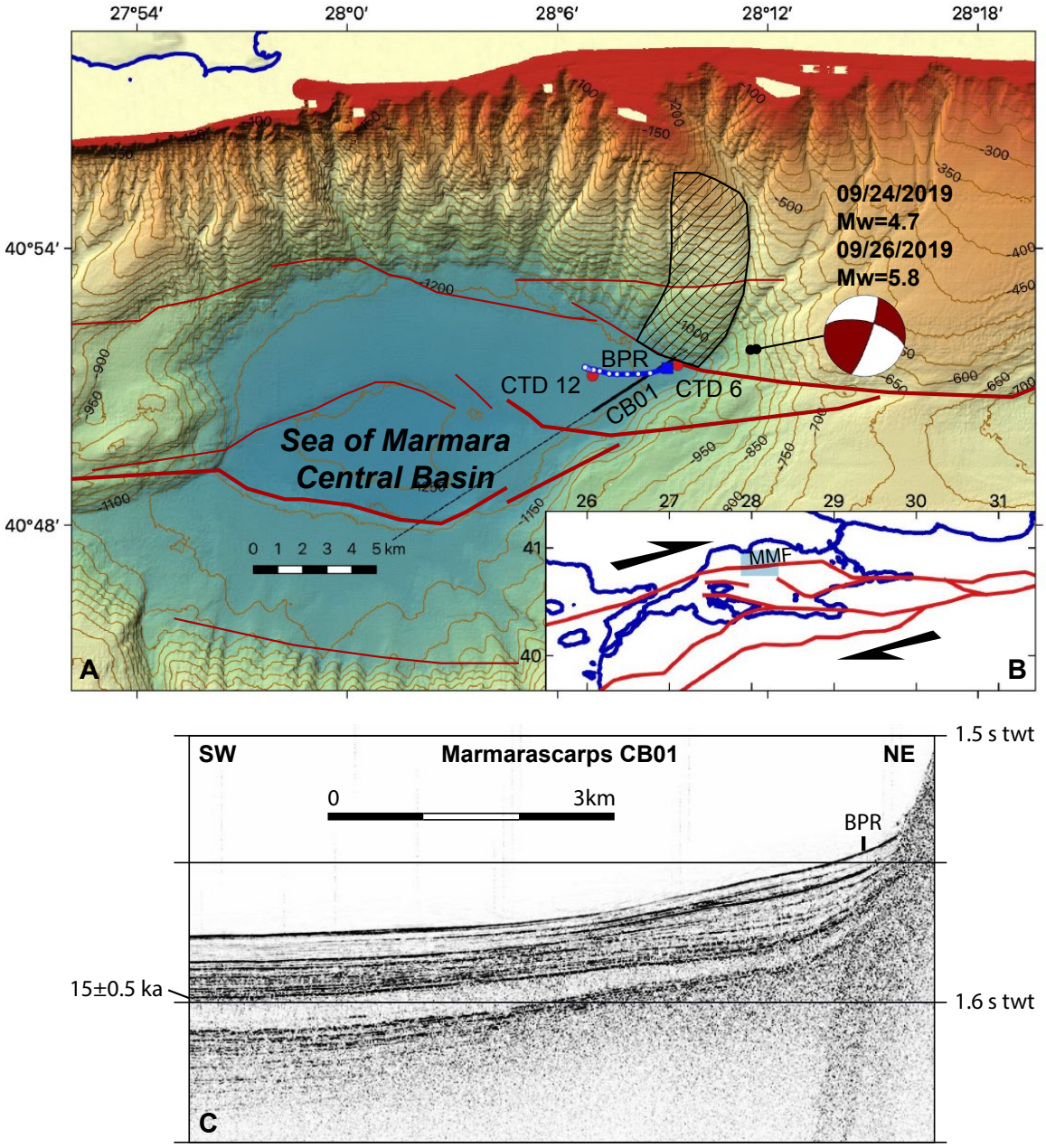


Figure 1. Context of instrumental deployment. (**A**) bathymetric map of the Sea of Marmara Central Basin with simplified fault geometry (in red). The hatched zone is a suspected mass wasting zone (Zitter et al., 2012). Location of instrumented frame comprising bottom pressure recorder (BPR) and doppler current meter is indicated by blue square. The blue banana with white dots represents the calculated trajectory of a sedimentary particle during the waning phase of the turbidity current. Red dots are CTD profiles 6 and 12 shown in supplementary material S1. Epicenter location of

earthquakes and the focal mechanism of the main shock are indicated. (**B**) Location of study area. North Anatolian Fault system is shown in red. MMF is the Main Marmara Fault. (**C**) Sediment sounder profile from Marmarascarps cruise (Armijo and Malavieille, 2002). Indicative age of reflector from Beck et al. (2007). The instrument (BPR) was deployed on a depositional fan at the base of slope and canyon outlet that differ in character from the hemipelagite / turbidite-homogenite sequence in the basin.

2. Context and data collection

A series of instrumental deployments was planned to record naturally occurring resonant water column oscillations (seiches) at various locations in the Sea of Marmara with the aim to improve tsunami models (Henry et al., 2021). An instrumented frame was thus deployed at 40.8568° N, 28.1523° E and 1184 m water depth in the Central Basin on May 9, 2019 and recovered 6 months later (11/19/2019) (Figure 1A). This site is located at the outlet of a branched canyon system originating from the edge of the continental shelf (Figure 1). Sediment sounder profiles indicate a depositional fan or lobe is present at this location (Figure 1C). The short canyons observed on the relatively steep sedimented slope (≈10°) of the Sea of Marmara deep basins are presumably fed by instabilities of the canyon heads and walls (Zitter et al. 2012; Çağatay et al., 2015). In addition, the slope west of the canyons immediately north of the deployment site hosts a mass wasting feature covering about 24 km^2 (Zitter et al. 2012). The Main Marmara Fault (MMF, Figure 1B), is defined as the part of the northern branch of the North Anatolian Fault system crossing the Sea of Marmara (Le Pichon et al., 2001, 2003). A splay of the MMF runs along the base of this slope (Armijo et al., 2002; Grall et al., 2012; Sengor et al., 2014). The 09/24/2019 and 09/26/2019 earthquakes occurred beneath the canyon system and their epicenters are located 5 km ENE of the instrument, less that 500 m apart (Figure 1). The rupture occurred within the crust at 9-13 km depth on a northward dipping fault located north of principal displacement zone of the Main Marmara Fault. The focal mechanism and aftershock distribution indicate right-lateral strike-slip with a reverse component (Karabulut et al., 2021). The rupture did not reach the seafloor, nor caused a tsunami. For instance, tidal gauge records obtained at Marmara Ereglisi do not deviate more than 1hPa from a fitted tidal model.

The instrumentation on the frame comprises (1) an RBR bottom pressure recorder (BPR) with a Paroscientific 0-2000 m Digiquartz sensor, (2) a Seaguard recording current meter (RCM) equipped with a Z-pulse 4520 Doppler current meter operating in the 1.9-2 MHz frequency range and other sensors: temperature, pressure (tide sensor Aanderaa 5217), conductivity (Aanderaa 4319), oxygen (Aanderaa optode 4330) (Figure 2). The RBR pressure recording interval was set to 5s and that of the Seaguard RCM to one hour for all sensors. The Doppler current meter worked in burst mode, averaging 150 pings taken every second at the end of each one-hour recording interval. The SeaGuard instrument was fixed on the upper part of the frame 1.5 m above the seafloor and emit 4 narrow (2°) beams at orthogonal directions in a plane, parallel to the seafloor if the frame is standing upright, and measures Doppler backscatter in cells extending 0.5-to-2 meters from the instrument (Figure 3). The instrument was set in forward ping mode, so that only data from sensors measuring a positive Doppler shift, upstream currents moving toward the instrument, are used to calculate current speed. The tide sensor is a piezoresistive sensor with a specified accuracy comparable to that of the Digiquartz sensors (4kPa for a 0-2000 m sensor vs. 2kPa for a Digiquartz sensor with the same range) and 0.2 hPa (2 mm) resolution and comprises a temperature sensor of 0.2°C accuracy and 0.001°C resolution. The tide sensor averages pressure measured at a 2 Hz sampling rate over 300 s at the end of each one-hour time interval. the tide sensor was checked against an atmospheric reference between deployments and found to have a minimal drift, less than 1 hPa.

As we will show that the 09/24/2019 earthquake caused the instrumented device to lay on its side for several hours and then straighten up, understanding the setup of the seafloor device and its stability is important (Figure 2B). The frame is made of aluminium and has 6 rigidly bound flotation spheres of 25 kg buoyancy each. The net weight of the instrumented frame in water is -80 kg. The frame is rigidly attached to a 12-cm-thick 1.5x1.3 m concrete slab, weighting 300 kg in water. The assembly of the heavy slab and buoyant frame is stable in upright position in the water and on the seafloor. Moreover, it is estimated that a current of 1 m/s would cause a total horizontal drag of 75 kg when the device is in upright position, which is insufficient to destabilize it. If a stronger current, or other external forces, cause the assembly to tilt and lay on one side, the moment of the gravity and buoyancy forces should straighten the device back to upright position when these external forces are removed.

Measurement of current speed and direction by a tilted instrument is a related issue that we here consider. The orientation and attitude of the Seaguard RCM is measured with a 2-component accelerometer and a magnetic compass and the recorded data include tilt in X and Y direction and the heading of the X axis. Tilt X and Y components are factory calibrated from -35° to +35° with an accuracy of 1.5°. Tests performed in the laboratory (see supplementary material, Figure S1) showed that tilt information remains consistent outside this range, even when the instrument is upside down. Tilt measurements are accurate within 3° up to 60° but saturate at about 80° (Figure S2). Uncertainty on heading also increases with tilt, especially when the instrument is tilted toward the X-direction. However, measured heading remains ±20° of true heading for a tilting of up to 60° (Figure S3). The current measured in the instrument plane is corrected for tilt assuming current is horizontal. As far as this approximation is valid, the current record should in principle remain fairly accurate when the instrument is tilted beyond the normal range of operation (±35° degree) and at least to 60°. However, the compass was not calibrated for an upside-down configuration. If the top of the instrument would happen to be oriented downward, the measured current direction will be unreliable, even though the absolute speed may still be correctly estimated. Another problem may arise if one of the Doppler sensors is facing down into the sediment so that its measurement cell is below the seafloor. If the sensor pointing upward in the opposite direction is recording a negative Doppler shift, this value will be ignored in the forward ping mode. In this case, the measurement retained to calculate current velocity will correspond to noise from the sensor facing toward the seafloor. In all situations, it remains possible to recalculate the sensor readings retained by the calculator from the current velocity and orientation parameters recorded by the instrument, and thus assess the reliability of data.

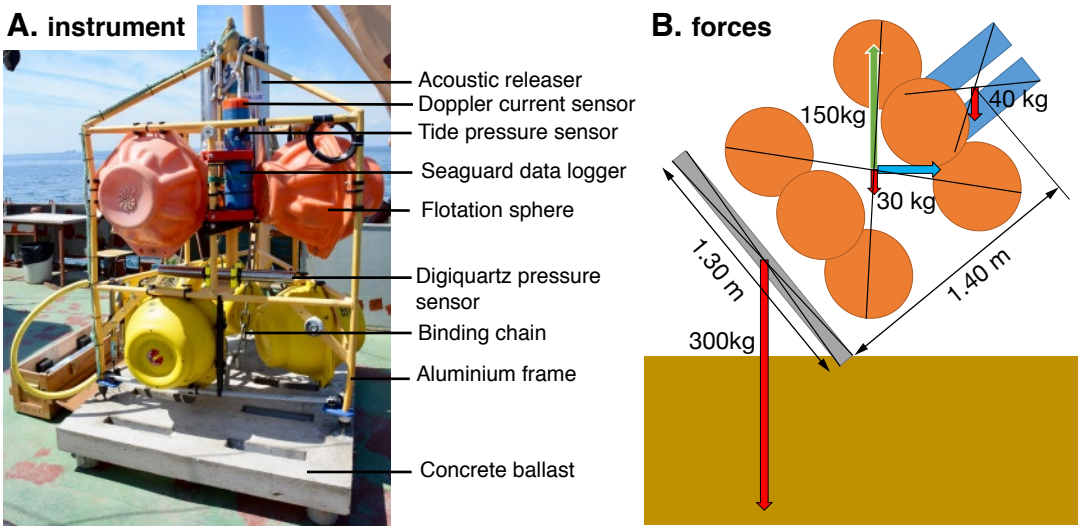


Figure 2. Instrumented frame. (A) photo of the instrumented frame before deployment. (B) Sketch showing forces applied to the elements of the instrumented frame in water. The red arrows represent the weight in water of the cement ballast, of the instrumented frame and of the acoustic release system on top. The green arrow represents the buoyancy of the flotation spheres. The blue arrow represents the current drag, which depends on current speed and instrument tilt.

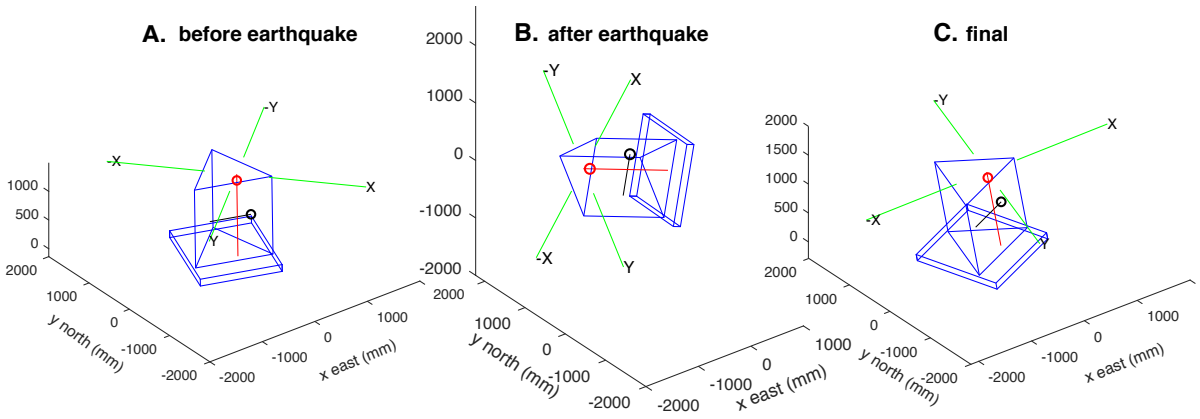


Figure 3. Reconstruction of frame position based on instrument tilt-meter and compass data: (A) before the earthquake; (B) Tilted, between, 25 minutes and 10.5 hours after earthquake; (C) back in nearly upright position 11 hours after earthquake. Position of Digiquartz pressure sensor (black circle), Aanderaa tide sensor (red circle) and Doppler current meter beam cells (green segments)

3. Results and interpretations

3.1. Pressure and tilt records

Pressure sensors are sensitive to pressure variations caused by P-waves and Digiquartz sensors are also intrinsically sensitive to acceleration, but to a small extent, 160 hPa/g for an instrument with 20 MPa range according to the calibration report. Small earthquakes are detected as pressure spikes, while oscillations are recorded after large earthquakes. The M_w 4.7 09/24/2019 caused a short pressure transient of 25 hPa at 08:00:26 followed by small pressure oscillations of less than 3 hPa amplitude decaying over a few minutes. The seismic wave train from the M_w 5.8, 09/26/1919 earthquake is recorded by the Digiquartz pressure sensor as oscillations, initiated by a pressure drop of 65 hPa between 10:59:22 and 10:59:26 (Figure 4). For the sampling interval of 5s used in this setup, the recorded signal is aliased, which precludes quantitative interpretation in term of velocity or acceleration. However, the initial pressure drop after the 09/26/1919 earthquake may indicate a negative polarity of the first P arrival at the instrument site, located on an ascending ray-path.

Twenty-five minutes after the M_w 5.8, earthquake, a new disturbance of the pressure sensor is observed at 11:23:41. The pressure then progressively increases by 30.9 hPa in 15 seconds between 11:24:46 and 11:25:01 before stabilizing. Over the corresponding one-hour-time-interval between successive records, the Seaguard RCM, initially subvertical (tilt less than 2°), acquires a strong tilt (Figure 3). At 11:57:48, measured tilt is -65° along the X-axis and +19° along the Y-axis, with X-axis in a N161° azimuth and these values remain constant ±2° over the next 10 hours, corresponding to an absolute tilt of 68° (Figure 4). The tilting of the instrument causes the Digiquartz and Tide sensors to record different pressure variations because they are located at different positions on the frame (Figure 2). Moreover, the pressure readings by the Digiquartz sensor also depend on its orientation relative to Earth gravity. Pressure at the Tide sensor location increases about 100 kPa, corresponding to a 1 m drop and indicating that the frame was then practically laying on its side. Ten hours later, the device apparently straightens itself in about 5 seconds, between 21:28:29 and 21:28:34 as indicated by a rapid pressure variation. After that, the recorded tilt parameters are moderate and stabilize at -11.5° for the X-axis and 5.3° for the Y-axis, with X-axis in a N105.3° azimuth.

The M_w 4.7 earthquake caused minor disturbances of the attitude of the instrument, with variations of tilt and heading of less than 0.5°. A M_w 3.6 foreshock of the M_w 5.8 occuring 26/09/2019 at 7:32 also caused minor disturbances. These indicate that the seafloor was sensitive to ground shaking caused by these small earthquakes, however, this did not cause the device to sink into the sediment. Changes of pressure baseline of the digiquartz sensor between before and after these earthquake are difficult to resolve, and correspond to less than 5 mm vertical displacement for the first event and less than 2 mm for the second one.

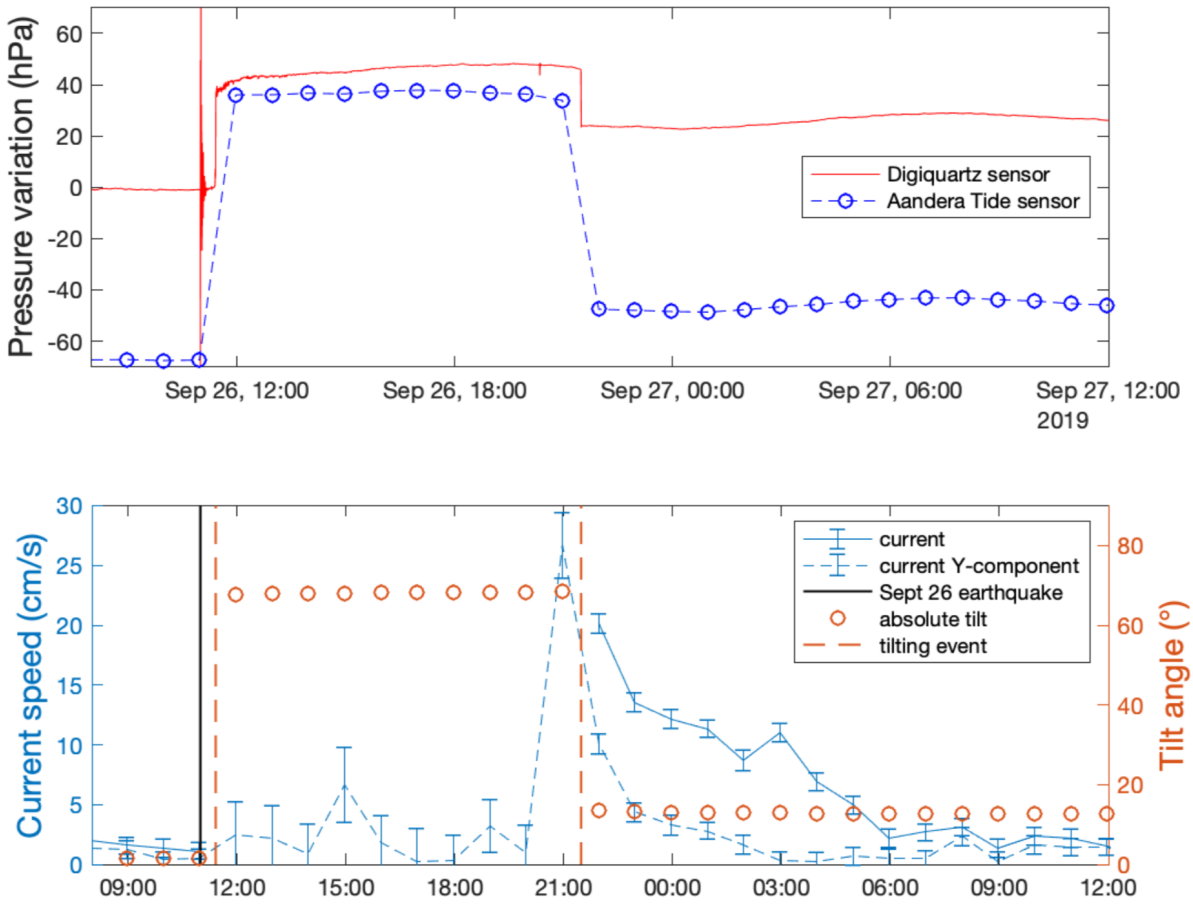


Figure 4. Time series around the time of occurrence of a M_w 5.8 earthquake; (top) pressure variations recorded by two instruments on the instrumented frame; (bottom) current and tilt data recorded by Seaguard RCM. Between the tilting events only one component of the doppler current meter functioned reliably (Y-component oriented N200) and is here reported.

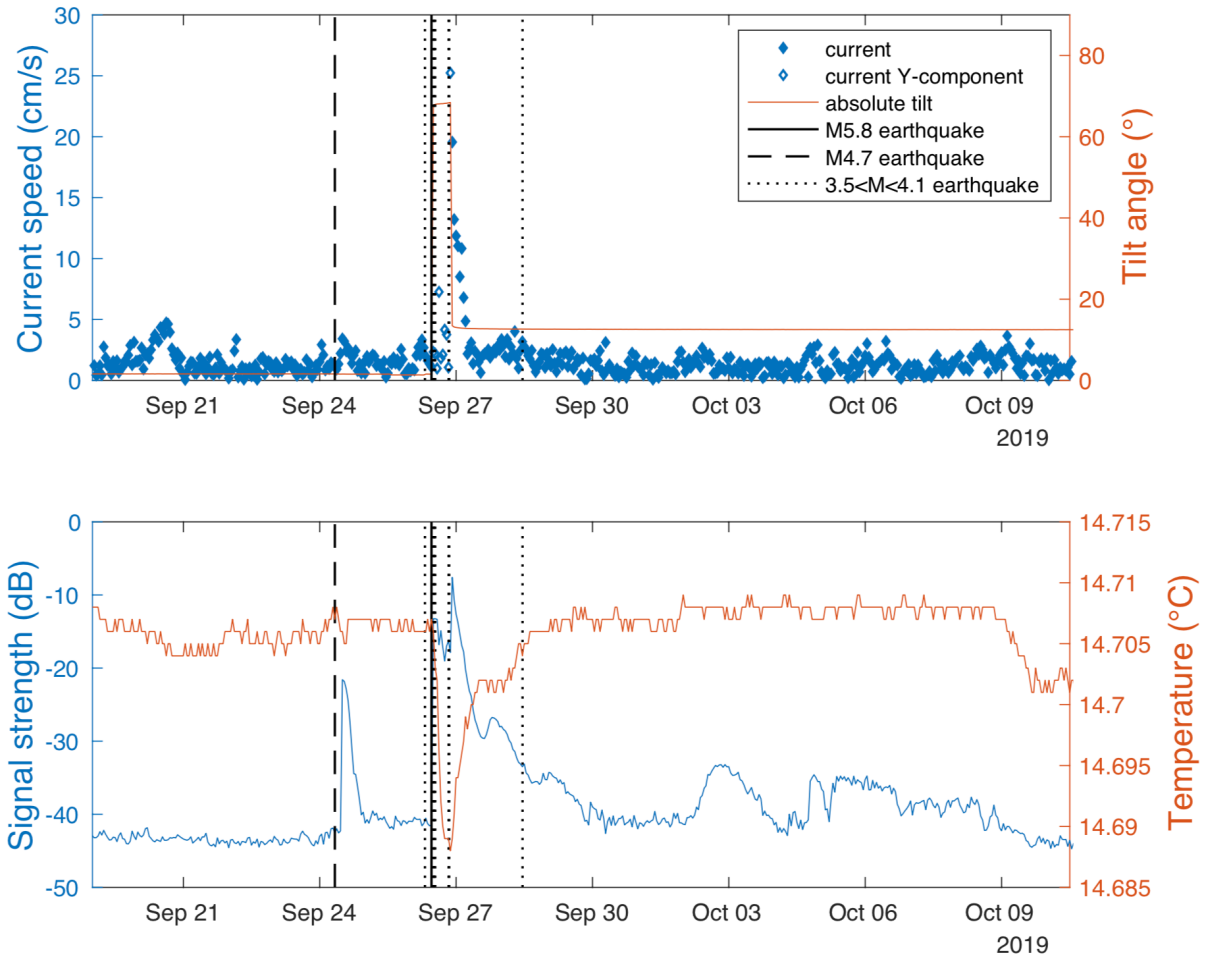


Figure 5. Time series acquired with Seaguard RCM during the September 2019 seismicity cluster; (top) current speed and tilt; (bottom) backscatter signal strength and temperature.

3.2. Current records and possible causes of tilting

The M_w 4.7 09/24/2019 earthquake was followed by a small increase of current strength peaking at 3.4 cm/s at noon, 4 hours after the earthquake (Figure 5). Comparable events in term of duration and strength occurred spontaneously 09/20/2019 (with currents up to 4.7 cm/s) and 09/26/2019 just before the main earthquake. During all three events the dominant current was from the east, thus coming from the direction of the canyon, but there is an important difference between the event that occurred after the earthquake and the two others. During that event a change in current direction occurred from eastward to westward between 10:57 and 11:57 while the current strength increased from 2.2 cm/s to its peak value (Figure 6). During the other events, build-up was more progressive and did not involve a change in direction. A drift plot, calculated by summing velocity vectors over time, reproduces

the motion of a particle assuming a uniform velocity field (Figure 6). The total drift is about 500 m and occurs in the 8 hours following the current inversion. Current direction varies from Westward to Northward during this time interval.

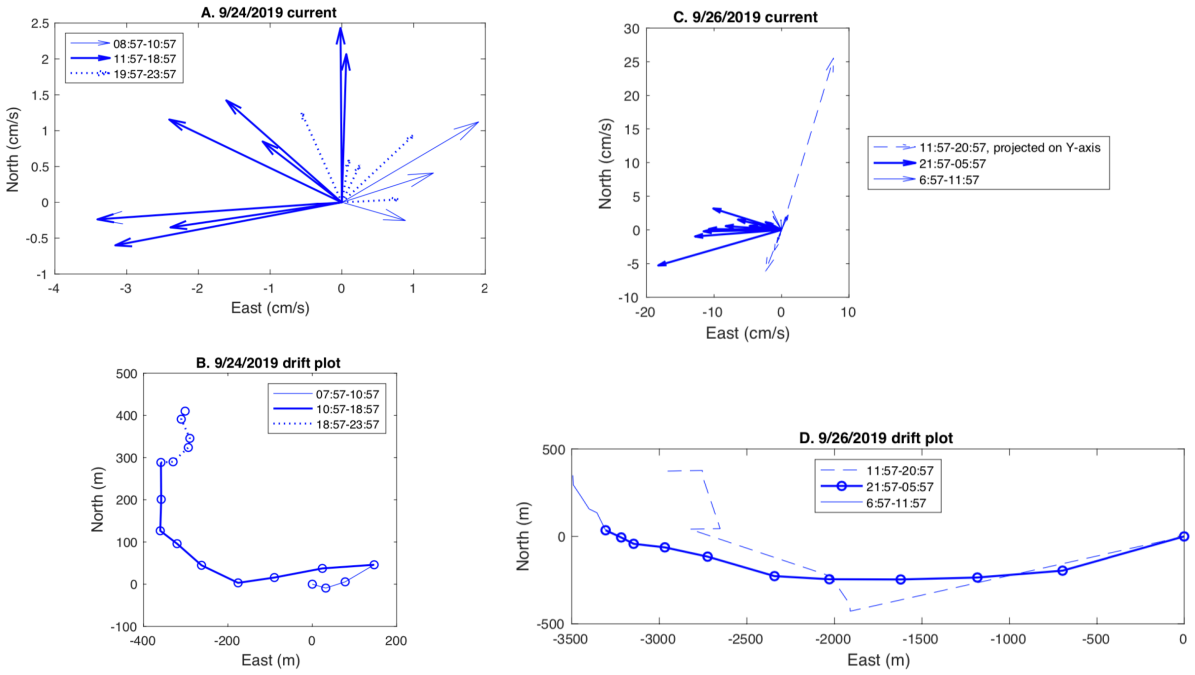


Figure 6. Current recorded after M_w 4.7 and M_w 5.8 earthquakes: (A) Current velocity arrows recorded every hour between 08:57 and 23:57 on 09/24/2019; (B) drift plot over the same time interval, the change of current direction and strength between 10:57 and 11:57 coincides with increasing backscatter strength (see figure 4), indicative of increased turbidity; (C) Current velocity arrows recorded every hour between 12:00 09/26/2019 and 06:00 09/27/2019. Dashed arrows show measurements acquired in the Y direction when the instrument was strongly tilted (position B in Figure 3), plain arrows when it was back in upright position (C in Figure 3); (D) drift plot over the same time interval, the dashed part corresponds to the strongly tilted position.

After the M_w 5.8 09/26/1919 earthquake, during the 10 hours period when the instrument remained strongly tilted, the instrument recorded currents varying both in speed and orientation, but some precautions are needed when interpreting these data. The current component measured by transducers along the Y-axis of the instrument, oriented N200°, probably remained accurate as the tilt along this axis is less than 20°

and the measurement cell remained above the bottom (Figure 2B). On the other hand, the X-component may not be reliable as one of the sensors (n°1) is oriented 65° upward in the N160° direction, and the oposite sensor (n°3) is dipping 65° downward in the opposite (N340°) direction. Consequently, measurement cell n°3 lies within the sediment and thus may only record noise. Moreover, because the Doppler current sensor (DCS) is set in forward pinging mode, current speed is calculated with data from sensors measuring positive doppler shifts only. This implies that if the current component toward N160° is positive, sensor n°1 will measure a negative shift and will not be recorded. During the time inteval here considered, the mesured current component in the X-direction (toward N160) is positive, which indicates that data from sensor n°4 was used (Figure 7), and that is probably noise. It follows that the current component along the Y-direction is the only one reliable. The horizontal current measured along the Y-axis changed sign several times during this time interval, and reached peak values of 6.3 cm/s toward N200 at 14:57:46, about four hours after the earthquake, and of 25 cm/s in the oposite direction at 20:57:46, the last measurement before the instrument straightenned up. Other measurements on both axes remain below 5 cm /s, but the absolute velocity may have been higher because this measurement was only performed in one direction. Yet, these observartions suggest that the strong current recorded before the instrument straightenned up played a role in this event. Once the device got back in an upright position, it recorded a current consistently flowing westward and progressively decreasing from 20 cm/s to background level (2 cm/s) in 9 hours (Figure 4). During this waning phase, the current drift is about 3.5 km in a westward direction (Figure 6). The drift estimated during the first 10 hours after the earthquake, while the instrument was strongly tilted, is in the opposite direction but may not be reliable.

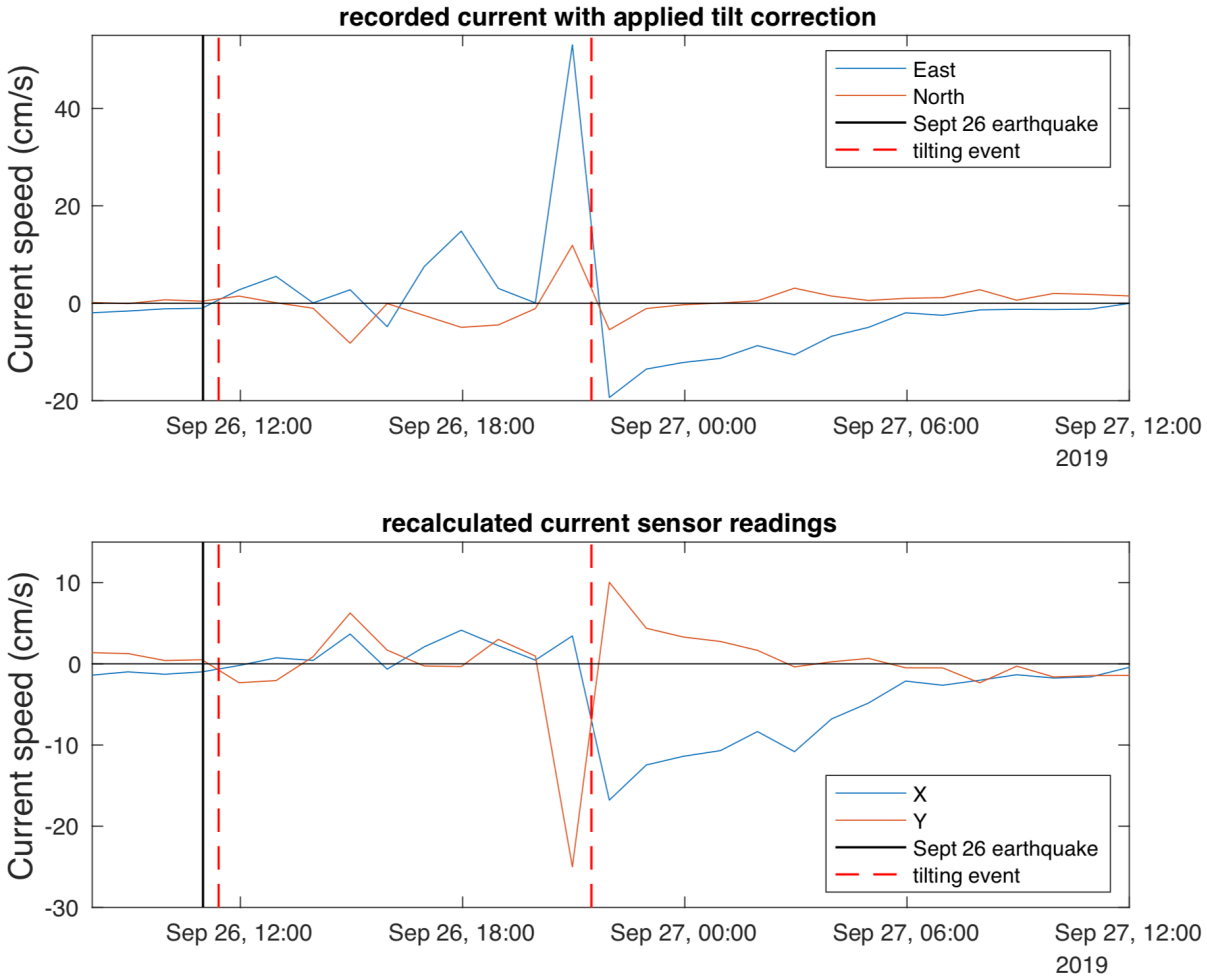


Figure 7. Current record acquired around the time of occurrence of a M_w 5.8 earthquake. A. Instrumental record, automatically corrected for tilt and heading. B. recalculated readings in the X and Y axis of the Doppler sensor (see text for interpretation).

The current speed in the first 2 hours after the main earthquake apparently remained low, at most 5-6 cm/s. It is thus unlikely that the tilt of the device was caused by strong currents. Some short burst of current may have been missed because of the 1 hour sampling interval, but this would not explain why the frame then remained stable in a tilted position for several hours. Local liquefaction of the sediment beneath the device is also an unlikely cause because the tilting of the instrument occurred 25 minutes after the earthquake. A mud flow originating from the basin slopes thus appears as a more likely cause. This hypothesis would also acount for the presence of sandy mud caked on the device in various places: on the frame feet, on the acoustic releasers, on the optode connector and also inside the plastic protection of a flotation

sphere, from which bindings were broken and had to be repaired. On the other hand, the current speed in the 20-50 cm/s range recorded before, as well as after, the time when the device straightened up is strong enough to cause erosion of mud or sand deposits. It may thus be hypothesized that erosion freed the device from the mud cover. The flotation spheres on the frame and the concrete ballast at its base exert a moment that should keep the assembly stable in an upright position unless the frame is loaded with sediment.

3.3. Acoustic backscatter record

The strength of the backscattered signal can be used as a proxy for turbidity. The Seaguard RCM emits in the 1.9-2 MHz band corresponding to a wavelength (λ) of 750 µm. Doppler backscatter current meters have maximum sensitivity for particles of diameter $D = \lambda/\pi$ and can detect particles down to diameter $D = 0.08\ \lambda$, for which backscatter power is less than 1/10 of peak backscatter power (Guerrero et al., 2011, 2012). The seaguard RCM should thus be mostly sensitive to the presence in suspension of sand size particles (larger than 63 µm). The background backscatter amplitude level is -43±1dB before the earthquakes. Three to four hours after the M_w 4.7 09/24/2019 earthquake, backscatter increases sharply to -22dB between 11:00 and 12:00, and then decays to -41dB in 12 hours. The increase of backscatter coincides with a change of current direction and speed, indicating that the turbid cloud was brought to the instrument site by the current. However, the current speed of less than 4 cm/s may have been insufficient to put the particles in suspension. There is no increase of backscatter on Sept 20 when stronger currents coming from the same direction, but not related with an earthquake, were recorded.

Backscatter strengh remain 41±1 dB the 1.5 days interval before the M_w 5.8 09/26/1919 and increases to the -20 dB to -13 dB range after the earthquake (Figure 5), which implies sand sized sediment was put in suspension soon after the earthquake although the local current speed remained relatively low (about 5 cm/s at most). After the device went back to near vertical position, signal strengh reaches a maximum of -7.6 dB, which correspond to an amplitude ratio of 42 and an intensity ratio of 1800 compared to base level. Similar signal strength levels are typically reached with the Z-Pulse sensor in highly turbid water such as in estuaries. During deep sea deployments signal strength range more typically between -60 and -40 dB. After reaching peak value,

backscattered signal strengh progressively decays to stabilise at about -40 dB 3 days (Figure 5). Several turbid events, with signal strength about -35 dB are observed in October and associated with small increases in current velocity (up to 3-4 cm/s). It is unclear whether these passing clouds are residual turbidity from the earthquake. After October 9, backscatter eventually returns to background level while temperature decreases by 0.007 °C over a few hours, indicating replacement of the water mass around the instrument.

3.4. Temperature record

The Sea of Marmara is stratified, with a low salinity (20-22‰) 20-30 m surface layer that displays strong seasonal temperature variability overlaying a high salinity (about 38‰) body of seawater at 14-15°C derived from the Aegean Sea (Beşiktepe et al., 1994). Within this body, the potential temperature generally decreases with depth, which would in principle imply that a turbidity current, flowing downward, should cause a small temperature increase. However, the deployment site is prone to seasonal cascading, so that the initial temperature structure may have been disturbed. Example of CTD profiles recorded in June 2007 (Henry et al., 2007) are shown in Figure 8. No CTD profile is available in Sept 2019, but variations in temperature and oxygen concentration associated with mild currents (<5 cm/s) were recorded by the instrument in May-July 2019, and again on Sept 20.

Temperature variations associated with the M_w 4.7 09/24/2019 earthquakes are very small, less than ±0.002°C, which confirms that water did not travel far during this event. After the M_w 5.8 09/26/1919 earthquake, the recorded temperature decreases progressively by about 0.015°C, after the first hydrologic disturbance and tilting of the instrument, until the recorded current reaches its maximum value (Figure 5). Temperature then progressively increases to reach nearly the same value as before the event. The small variation in temperature recorded indicates that the turbid water originates from the deep-water body. The slight temperature decrease observed after the earthquake can result from the mixing of a warmer bottom water layer with the bulk of the deep-water layer. However, the observation of a temperature drop precludes that the turbid water originates from depths less than 400 m, as water present between 400 m and the halocline is at a higher potential temperature than the deeper water throughout the year (see Beşiktepe et al., 1994, and figure 8). Moreover, an inflow of

water from closer to the surface should result in an increase in the O_2 concentration in the bottom water, but none is observed in the data.

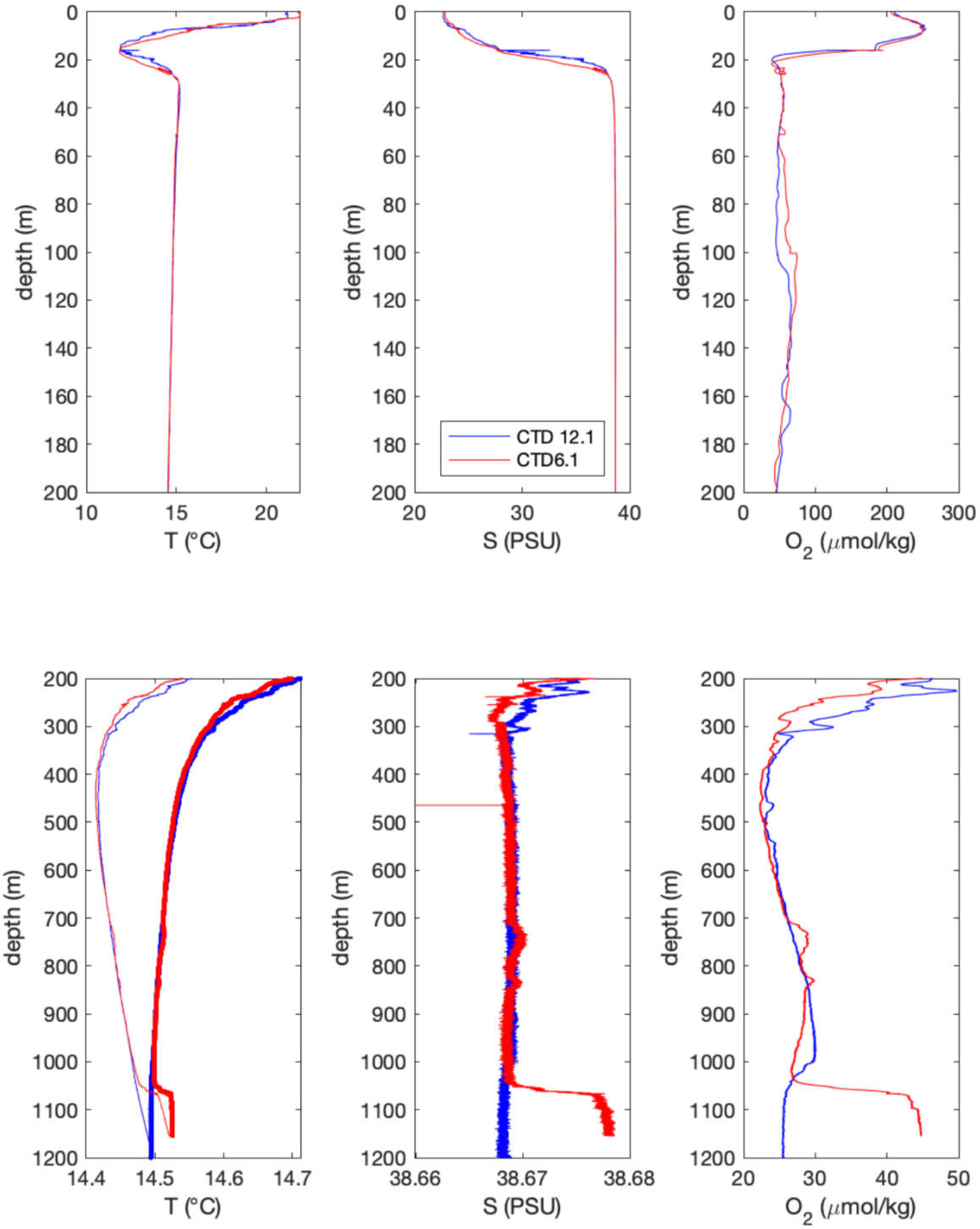


Figure 8. Depth plots of Temperature (°C), Salinity (PSU) and oxygen concentration (µmol/kg) from CTD profiles acquired in the Sea of Marmara during Marnaut cruise of Ifremer RV L'Atalante (Henry et al., 2007). On the lower temperature plot, thin lines

419 are measured values and thick lines are potential temperatures calculated at 1180 m.
420 Locations are shown on Figure 1
421
422 ### 3.5. Inferred sequence of events
423 These observations provide some insight on the complex sequence of events
424 that followed the earthquake and suggest the following scenario. After the M_w 4.7
425 09/24/2019 a turbid cloud formed east of the instrument and drifted slowly. Considering
426 the maximum velocity of the current (less than 4 cm/s) and the 4-hours interval
427 between the earthquake and the passing of the turbid cloud over the instrument, the
428 front of turbid water should have formed ENE of the instrument at a maximum distance
429 of about 500 m, and this coincides with the base of the northern slope near the outlet
430 of the canyon. It is suspected that instability on the steeper slopes on the sides of the
431 canyon is the primary cause of sediment suspension. The clouds subsequently drifted
432 downslope over a total horizontal distance of at most 1 kilometers before dissipating,
433 adding the 500 m estimate above to the drift calculated after the passing of the front
434 over the instrument (Figure 6).
435 The M_w 5.8 09/26/1919 caused much stronger currents. After the passing of
436 the seismic wave, triggering of instability on slopes adjacent to the deployment site
437 caused mud flows that spread on the basin floor causing the tilting of the instrument
438 25 minutes after the earthquake, and bottom water turbidity. As the base of the nearest
439 slope is about 400 m north of the instrument, this would imply a minimum velocity of
440 20 cm/s for the mudflow to reach the device location in 25 minutes. During the following
441 10 hours, the current record is incomplete but indicates variations in strength and
442 direction. Widespread slope instabilities triggered by the earthquake may have resulted
443 in several turbidity currents recorded as succesive pulses. The role of seiches and
444 surface gravity waves in sediment resuspension can be ruled out as no tsunami was
445 recorded by near shore tidal gauges around the Sea of Marmara. The relationship
446 between gravity wave amplitude A and bottom current amplitude U in the shallow water
447 linear approximation is given by $U=(g/H)^{1/2}A$, where H is water column height. An
448 oscillatory current of 10 cm/s at 1200 m depth would thus correspond to a free surface
449 oscillation of 1 m (or 100 hPa) for a standing wave (seiche) as well as a progressive
450 wave (tsunami). This should have been easily detected in a sea where tidal amplitude
451 is about 10 cm (Alpar and Yüce, 1998). The influence of baroclinic internal waves on

452 the halocline at 20-30 m depth must also be ruled out as they cannot physically
453 produce currents of more than a few cm/s at 1200 m. However, It remains possible
454 that the interface at the top of the turbid cloud is affected by baroclinic waves. The
455 strongest current is recorded after 10 hours, which suggests that a turbidity current
456 initiated further upslope may have reached the site after a longer delay but may also
457 have gained more kinetic energy on its downhill path. This event, reaching a speed
458 exceeding 25 cm/s apparently caused enough erosion to free the device from the mud
459 accumulation. The current then stabilizes in a westward direction and decays
460 progressively over the next 9 hours, which suggests the tail of a turbidity current flowing
461 in the canyon E of the deployment site has been recorded. The hours-long delay
462 between the earthquake and the passing of the fastest current over the instrument may
463 hypothetically correspond to the time for the head of the turbidity current to travel from
464 its source to the location of the instrument. The length of the canyon valley between
465 the device location and the 400 m isobath, inferred to be the minimum depth of the
466 turbid water source, is about 13 km. In this scenario, the average velocity of the head
467 of the turbidity current would be 30-40 cm/s. Alternatively, a sequence of slope failures
468 may have lasted up to several hours after the earthquake. The distance travelled by
469 the turbidity current on the basin floor beyond the instrument may be estimated from
470 the calculated drift during the waing phase, and is found to be about 3.5 km (Figure 6).
471 When plotted over the bathymetric map the drift appears to stay within the depositional
472 fan at the outlet of the cayon, the extension of which is known from sediment sounder
473 profiles (Figure 1). These calculations are only a rough estimate of the distance
474 travelled by suspended particles as only the velocity at 1.5 m above the seafloor is
475 known. However, it appears unlikely that sediments spread all over the 15x20 km basin
476 floor as this would require velocities of the order of 1m/s, sustained over a wide area
477 for several hours.
478 The decay of the backscatter signal strength over the next 3 days may reflect
479 the settling of sand size particles put in suspension in the water column after this
480 sequence of events. For a first order assessment, Stokes settling velocity, an upper
481 bound valid in dilute suspensions (e.g. Guazelli and Morris, 2012) may be used. The
482 Stokes settling velocity of 63 µm quartz grains (density 2650 kg/m^3) in 13°C seawater
483 is 2.7 mm/s, allowing such grains to drop by 700 m in 3 days. However, if the particles
484 forming the cloud are mostly composed of clay agregates, which density may be
485 comprised between 1200 and 1700 kg/m^3, the settling velocity would be comprised

between 0.3 mm and 1 mm/s. In this case the height of the suspended particle cloud could range between 70 and 250 m.

4. Discussion and conclusion

Data obtained with a seafloor device located at the oultet of a canyon in the Central Basin in the Sea of Marmara bring some insight on how earthquakes scale with their hydrodynamic consequences. In September 2019, M_w 4.7 and 5.8 earthquakes occurred at a 5 km distance from the device as well as a series of smaller foreshocks and aftershocks In this setting, earthquakes of magnitude less than 4 did not cause noticeable water column turbidity nor currents. The M_w 4.7 earthquake generated a turbid cloud on slopes a few hundred meters from the instrument and the cloud took 3-4 hours to drift down to the instrument location and 10 more hours to dissipate. As the current velocity remained small (less than 4 cm/s), it can be concluded that this cloud did not evolve into a self-sustained turbidity current (Parker, 1982). The M_w 5.8 earthquake initiated a turbidity current and the data obtained may be compared with more complete records of turbidity currents obtained elsewhere with ADCP deployments and/or water column mooring lines. The duration of the event in the Sea of Marmara (about 10 hours) appear fairly typical and comparable with events recorded in other locations regardless of the initiation mechanism, which comprise hyperpycnal flows from river floods (Var and Gaoping canyons), storm waves and dredging (Gulf of St Laurence and Monterey canyon), and slope instabilities triggered by an earthquake (Tokachi-oki) or by other processes (Var canyon) (Normandeau et al., 2019; Khripounoff et al., 2012; Xu et al., 2004; Liu et al., 2012; Mikada et al., 2006). Longer duration events with very different hydrodynamic characteristics have been observed in larger scale systems (e.g. Congo deep sea canyon, Azpiroz-Zabala et al., 2017). On the other hand, events recorded closer to shore on the edge of the continental shelf or on a delta front have much shorter durations (Xu et al., 2010; Hughes Clarke, 2016). In events of comparable scale to the Sea of Marmara one, the velocity of the current generally reaches its maximum several meters above the seafloor, so that the velocity recorded by our instrument at 1.5 m from the seafloor is within the boundary layer, and lower than either the maximum current velocity or the velocity of the head of the turbidity current. A velocity of several tens of centimeter per second is representative of the slower recorded examples, corresponding to mud rich flows associated with hyperpycnal flows, to the smaller landslides (Khripounoff et al. 2012) or to the smaller

519 storm-related events (Normandeau et al., 2019). Turbidites following large
520 earthquakes or large slope instabilities have reached maximum velocities of 20 m/s
521 (Piper et al., 1999). Velocities of 2-7 m/s were reported for the turbidity current following
522 Tohoku earthquake (Arai et al., 2013) and 1.4 m/s in the Tokachi-Oki case (Mikada et
523 al., 2006). The downward current after the off-Izu Penninsula earthquake may be
524 constrained with a noisy ADCP record to a maximum of 10-15 cm/s in a 20-30 m layer
525 above the seafloor and lasted about one hour, peaking about 30 minutes after the
526 earthquake (Kasaya et al., 2009). This turbidity current thus appears less intense and
527 shorter in duration than the one recorded in the Sea of Marmara, but the triggering
528 earthquake was also smaller (M5.4 compared to M5.8) and more distant (10 km).
529 These observations suggest that a general scaling relationship could exist between
530 earthquake magnitudes and the strength and extent of the turbidity currents they
531 induce. Moreover, although the off-Izu event is shorter than the Sea of Marmara one,
532 they share an important characteristic in that the turbid cloud is observed to form when
533 a mud flow hits the observatory site and some time before current builds up in the
534 water column.

535 The 10 hours delay observed in the Sea of Marmara between the triggering
536 event and the peak of the turbidity current is long compared to the 2 hours delay
537 observed after Tohoku and Tokachi-oki earthquakes. We suggested earlier that the
538 long delay may simply result from a slower velocity of the turbidity current or from
539 delayed slope failure. Another possibility is delayed ignition, which may occur if the
540 turbidity current develops indirectly from the hydrodynamic instability of a turbid cloud
541 resulting from slope failures and/or ground shaking rather than by acceleration of a
542 dense mud flow (Parker, 1982; Mulder and Cochonnat, 1996; Piper and Normark,
543 2009).

544 The scenario we propose for the Sept 26, 2019 earthquake involving mud flows
545 from proximal sources, followed by turbidity currents originating at larger distances,
546 and the subsequent settling of sediment in suspension, could relate with the structure
547 of turbidite-homogenites. Progressive or pulsed build-up of turbidity current energy is
548 considered typical of hyperpycnal flows initiated by river floods (Mulder et al., 2003)
549 but reverse grading and pulsing is also observed in seismoturbidites (Gutierrez-Pastor
550 et al., 2013). In the Sea of Marmara, many of the laminated turbidites sampled in
551 Kumburgaz Basin formed from the amalgamation (below the homogenite layer) of at
552 least two flows, the first one being finer and less sorted (Yakupoğlu et al., 2019). The

coarsening observed in this context is often associated with an increase of the calcium content indicative of a shallower source, rich in biogenic carbonate material. However, in the case observed in the present study, remobilization of sediment should be limited to the lower slope as the temperature of the displaced water precludes a source shallower than 400 m water depth.

The geomorphological context of the deployment site south of a slope identified as unstable from geomorphological criteria (Zitter et al., 2012), and on a depositional fan at the outlet of a canyon is also consistent with the proposed scenario. We estimated by integrating recorded current velocity that the current during this event was not strong enough to spread the sediment over the entire Central Basin floor but that the zone of deposition was probably comparable in size to the fan. It can be inferred that the paleoseismological record from a core taken in the fan should contain more events than one taken at the basin depocenter. A sediment sounder profile (Figure 1) also shows that the character of the seismic reflectors differs in the basin and in the fan and that establishing reliable correlations between them is not simple. However, as hypothesized by previous studies (McHugh et al., 2014), turbidite-homogenite deposits that can be correlated between cores taken at various locations in the basin probably correspond to the larger events, which may be correlated with historical earthquakes. Moreover, it is still unknown whether the Sept 26 event left a trace on the seafloor morphology and in the sediment record. Performing new core sampling and very high-resolution geophysical surveys in this area would thus have important implications for the understanding of seismoturbidite records and for the assessment of geohazards.

Acknowledgements

Financial support was provided by the bilateral ANR/TÜBITAK collaborative research project MAREGAMI (ANR-16-CE03-0010-02 and Tübitak Project 116Y371) and by CNRS-INSU through the European Multidisciplinary Sea Observatory (EMSO) Research Infrastructure program. DT-INSU and Istanbul Technical University hydrodynamic engineering department provided technical support for device design, construction, and deployment. Bernard Mercier de Lépinay provided processed sediment sounder profiles. We thank the crew and Captain of R/V Yunus (Istanbul University) for their support during installation and recovery of the instruments.

Seafloor monitoring data are available through SEANOE (Henry et al., 2021) and CTD profile data through SISMER Oceanographic Data portal (Henry et al., 2007).

References

Alpar, B., & Yüce, H. (1998). Sea-level variations and their interactions between the Black Sea nd the Aegean Sea. Estuarine, Coastal and Shelf Science, 46, 609–619.

Arai, K., Naruse, H., Miura, R., Kawamura, K., Hino, R., Ito, Y., Inazu, D., Yokokawa, M., Izumi, N., Murayama, M., & Kasaya, T. (2013). Tsunami-generated turbidity current of the 2011 Tohoku-Oki earthquake. Geology, 41(11), 1195–1198. https://doi.org/10.1130/G34777.1

Armijo, R., Meyer, B., Navarro, S., King, G., & Barka, A. (2002). Asymmetric slip partitioning in the Sea of Marmara pull-apart: a clue to propagation processes of the North Anatolian Fault? Terra Nova, 14(2), 80–86. https://doi.org/10.1046/j.1365-3121.2002.00397.x

Armijo, R. and J. Malavieille (2002) MARMARASCARPS cruise, RV L'Atalante, https://doi.org/10.17600/2010140

Azpiroz-Zabala, M., Cartigny, M. J. B., Talling, P. J., Parsons, D. R., Sumner, E. J., Clare, M. A., Simmons, S. M., Cooper, C., & Pope, E. L. (2017). Newly recognized turbidity current structure can explain prolonged flushing of submarine canyons. Science Advances, 3(10). https://doi.org/10.1126/sciadv.1700200

Beck, C., Mercier de Lépinay, B., Schneider, J. L., Cremer, M., Çağatay, N., Wendenbaum, E., et al. (2007). Late Quaternary co-seismic sedimentation in the Sea of Marmara's deep basins. Sedimentary Geology, 199, 65–89. https://doi.org/10.1016/j.sedgeo.2005.12.031

Beşiktepe, Ş. T., Sur, H. İ., Özsoy, E., Latif, M. A., Oğuz, T., & Ünlüata, Ü. (1994). The circulation and hydrography of the Marmara Sea. Progress in Oceanography, 34(4), 285–334. https://doi.org/10.1016/0079-6611(94)90018-3

Brizuela, N., Filonov, A., & Alford, M. H. (2019). Internal tsunami waves transport sediment released by underwater landslides. Scientific Reports, 9(1), 10775. https://doi.org/10.1038/s41598-019-47080-0

Bulut, F., Aktuğ, B., Yaltırak, C., Doğru, A., & Özener, H. (2019). Magnitudes of future large earthquakes near Istanbul quantified from 1500 years of historical earthquakes, present-day microseismicity and GPS slip rates. Tectonophysics, 764(July 2018), 77–87. https://doi.org/10.1016/j.tecto.2019.05.005

Çağatay, M. N., Erel, L., Bellucci, L. G., Polonia, a., Gasperini, L., Eriş, K. K., Sancar, Ü., Biltekin, D., Uçarkuş, G., Ülgen, U. B., & Damci, E. (2012). Sedimentary earthquake

records in the İzmit Gulf, Sea of Marmara, Turkey. Sedimentary Geology, 282, 347–359. https://doi.org/10.1016/j.sedgeo.2012.10.001

Çağatay, N. M., Ucarkus, G., Eris, K. K., Henry, P., Gasperini, L., & Polonia, A. (2015). Submarine canyons of the Sea of Marmara. In F. Briand (Ed.), Submarine Canyon Dynamics in the Mediterranean and Tributary Seas, CIESM Workshop Monograph n° 47 (pp. 123–135). CIESM Publisher, Monaco. https://doi.org/10.13140/RG.2.1.1692.8402

Cattaneo, A., Babonneau, N., Ratzov, G., Dan-Unterseh, G., Yelles, K., Bracane, R., Mercier De Lapinay, B., Boudiaf, A., & Daverchare, J. (2012). Searching for the seafloor signature of the 21 May 2003 Boumerdas earthquake offshore central Algeria. Natural Hazards and Earth System Science, 12(7), 2159–2172. https://doi.org/10.5194/nhess-12-2159-2012

Dan, G., Sultan, N., Savoye, B., Deverchere, J., & Yelles, K. (2009). Quantifying the role of sandy-silty sediments in generating slope failures during earthquakes: Example from the Algerian margin. International Journal of Earth Sciences, 98(4), 769–789. https://doi.org/10.1007/s00531-008-0373-5

Drab, L., Hubert Ferrari, A., Schmidt, S., & Martinez, P. (2012). The earthquake sedimentary record in the western part of the Sea of Marmara, Turkey. Natural Hazards and Earth System Science, 12(4), 1235–1254. https://doi.org/10.5194/nhess-12-1235-2012

Drab, L., Hubert-Ferrari, A., Schmidt, S., Martinez, P., Carlut, J., & El Ouahabi, M. (2015). Submarine Earthquake History of the Çınarcık Segment of the North Anatolian Fault in the Marmara Sea, Turkey. Bulletin of the Seismological Society of America, 105(2A), 622–645. https://doi.org/10.1785/0120130083

Eriş, K. K., Çağatay, N., Beck, C., Mercier de Lepinay, B., & Corina, C. (2012). Late-Pleistocene to Holocene sedimentary fills of the Çinarcik Basin of the Sea of Marmara. Sedimentary Geology, 281, 151–165. https://doi.org/10.1016/j.sedgeo.2012.09.001

Garfield, N., Rago, T. A., Schnebele, K. J., & Collins, C. A. (1994). Evidence of a turbidity current in Monterey Submarine Canyon associated with the 1989 Loma Prieta earthquake. Continental Shelf Research, 14(6), 673–686. https://doi.org/10.1016/0278-4343(94)90112-0

Goldfinger, C., Nelson, C. H., & Johnson, J. E. (2003). Holocene earthquake records from the cascadia subduction zone and northern san andreas fault based on precise dating of offshore turbidites. Annual Review of Earth and Planetary Sciences, 31(1), 555–577. https://doi.org/10.1146/annurev.earth.31.100901.141246

Goldfinger, C., Nelson, C. H., Morey, A. E., Johnson, J. E., Patton, J., Karabanov, E., Gutiérrez-Pastor, J., Eriksson, A. T., Gràcia, E., Dunhill, G., Enkin, R. J., Dallimore, A., & Vallier, T. (2012). Earthquake Hazards of the Pacific Northwest Coastal and Marine Regions Turbidite Event History — Methods and Implications for Holocene

Paleoseismicity of the Cascadia Subduction Zone Professional Paper 1661 – F. USGS, Professional Paper 1661-F, 170. Retrieved from http://pubs.usgs.gov/pppp1661f/

Grall, C., Henry, P., Tezcan, D., Mercier de Lepinay, B., Becel, A., Geli, L., Rudkiewicz, J.-L., Zitter, T., & Harmegnies, F. (2012). Heat flow in the Sea of Marmara Central Basin: Possible implications for the tectonic evolution of the North Anatolian fault. Geology, 40(1), 3–6. https://doi.org/10.1130/G32192.1

Guazzelli, E., Morris, J. F., & Pic, S. (2011). A Physical Introduction to Suspension Dynamics. Cambridge: Cambridge University Press. https://doi.org/10.1017/CBO9780511894671

Guerrero, M., Rüther, N., & Szupiany, R. N. (2012). Laboratory validation of acoustic Doppler current profiler (ADCP) techniques for suspended sediment investigations. Flow Measurement and Instrumentation, 23(1), 40–48. https://doi.org/10.1016/j.flowmeasinst.2011.10.003

Guerrero, M., Szupiany, R. N., & Amsler, M. (2011). Comparison of acoustic backscattering techniques for suspended sediments investigation. Flow Measurement and Instrumentation, 22(5), 392–401. https://doi.org/10.1016/j.flowmeasinst.2011.06.003

Gutiérrez-Pastor, J., Nelson, C. H., Goldfinger, C., & Escutia, C. (2013). Sedimentology of seismo-turbidites off the Cascadia and northern California active tectonic continental margins, northwest Pacific Ocean. Marine Geology, 336, 99–119. https://doi.org/10.1016/j.margeo.2012.11.010

Hébert, H., Schindelé, F., Altinok, Y., Alpar, B., & Gazioglu, C. (2005). Tsunami hazard in the Marmara Sea (Turkey): A numerical approach to discuss active faulting and impact on the Istanbul coastal areas. Marine Geology, 215, 23–43. https://doi.org/10.1016/j.margeo.2004.11.006

Heezen, B. C., Ericson, D. B., & Ewing, M. (1954). Further evidence for a turbidity current following the 1929 Grand banks earthquake. Deep Sea Research (1953), 1(4), 193–202. https://doi.org/10.1016/0146-6313(54)90001-5

Henry, P., A.M.C. Şengör, M.N. Çağatay (2007) MARNAUT cruise, RV L'Atalante, https://doi.org/10.17600/7010070

Henry, P., Özeren M.S., Desprez De Gesincourt O., de Saint-Leger E., Libes,, M., Çakir, Z., Yakupoğlu, N., Géli, L. (2021). EMSO / MAREGAMI Marmara bottom pressure and current records. SEANOE. https://doi.org/10.17882/78928

Hsu, S. K., Kuo, J., Lo, C. L., Tsai, C. H., Doo, W. Bin, Ku, C. Y., & Sibuet, J. C. (2008). Turbidity currents, submarine landslides and the 2006 Pingtung earthquake off SW Taiwan. Terrestrial, Atmospheric and Oceanic Sciences, 19(6), 767–772. https://doi.org/10.3319/TAO.2008.19.6.767(PT)

694 Hughes Clarke, J. E. (2016). First wide-angle view of channelized turbidity currents links
695 migrating cyclic steps to flow characteristics. Nature Communications, 7(1), 11896.
696 https://doi.org/10.1038/ncomms11896
697 Ikehara, K., Kanamatsu, T., Nagahashi, Y., Strasser, M., Fink, H., Usami, K., et al. (2016).
698 Documenting large earthquakes similar to the 2011 Tohoku-oki earthquake from
699 sediments deposited in the Japan Trench over the past 1500 years. Earth and Planetary
700 Science Letters, 445, 48–56. doi:10.1016/j.epsl.2016.04.009
701 Karabulut, H., Güvercin, S. E., Eskikoÿ, F., Konca, A. Ö., & Ergintav, S. (2021). The
702 moderate size 2019 September Mw5.8 Silivri earthquake unveils the complexity of the
703 Main Marmara Fault shear zone. Geophysical Journal International, 224(1), 377–388.
704 https://doi.org/10.1093/gji/ggaa469
705 Kasaya, T., Mitsuzawa, K., Goto, T., Iwase, R., Sayanagi, K., Araki, E., Asakawa, K., Mikada,
706 H., Watanabe, T., Takahashi, I., & Nagao, T. (2009). Trial of Multidisciplinary
707 Observation at an Expandable Sub-Marine Cabled Station “Off-Hatsushima Island
708 Observatory” in Sagami Bay, Japan. Sensors, 9(11), 9241–9254.
709 https://doi.org/10.3390/s91109241
710 Khripounoff, A., Crassous, P., Lo Bue, N., Dennielou, B., & Silva Jacinto, R. (2012). Different
711 types of sediment gravity flows detected in the Var submarine canyon (northwestern
712 Mediterranean Sea). Progress in Oceanography, 106, 138–153.
713 https://doi.org/10.1016/j.pocean.2012.09.001
714 Le Pichon, X., Chamot-Roooke, N., Rangin, C., & Sengör, A. M. C. (2003). The North
715 Anatolian fault in the Sea of Marmara. Journal of Geophysical Research, 108, 2179.
716 https://doi.org/10.1029/2002JB001862
717 Le Pichon, X., Şengör, A. M. C., Demirbağ, E., Rangin, C., İmren, C., Armijo, R., Görür, N.,
718 Çağatay, N., Mercier de Lepinay, B., Meyer, B., Saatçılar, R., & Tok, B. (2001). The
719 active Main Marmara Fault. Earth and Planetary Science Letters, 192(4), 595–616.
720 https://doi.org/10.1016/S0012-821X(01)00449-6
721 Liu, J. T., Wang, Y.-H., Yang, R. J., Hsu, R. T., Kao, S.-J., Lin, H.-L., & Kuo, F. H. (2012).
722 Cyclone-induced hyperpycnal turbidity currents in a submarine canyon. Journal of
723 Geophysical Research: Oceans, 117(C4), n/a-n/a.
724 https://doi.org/10.1029/2011JC007630
725 McHugh, C. M. G., Seeber, L., Cormier, M. H., Dutton, J., Cagatay, N., Polonia, A., Ryan, W.
726 B. F., & Gorur, N. (2006). Submarine earthquake geology along the North Anatolia Fault
727 in the Marmara Sea, Turkey: A model for transform basin sedimentation. Earth and
728 Planetary Science Letters, 248, 661–684. https://doi.org/10.1016/j.epsl.2006.05.038
729 McHugh, C. M., Seeber, L., Braudy, N., Cormier, M. H., Davis, M. B., Diebold, J. B.,
730 Dieudonne, N., Douilly, R., Gulick, S. P. S., Hornbach, M. J., Johnson, H. E., Mishkin, K.

731 R., Sorlien, C. C., Steckler, M. S., Symithe, S. J., & Templeton, J. (2011). Offshore
732 sedimentary effects of the 12 January 2010 Haiti earthquake. Geology, 39(8), 723–726.
733 https://doi.org/10.1130/G31815.1
734 McHugh, C. M. G., Braudy, N., Çağatay, M. N., Sorlien, C., Cormier, M.-H., Seeber, L., &
735 Henry, P. (2014). Seafloor fault ruptures along the North Anatolia Fault in the Marmara
736 Sea, Turkey: Link with the adjacent basin turbidite record. Marine Geology, 353, 65–83.
737 https://doi.org/10.1016/j.margeo.2014.03.005
738 Mikada, H., Mitsuzawa, K., Matsumoto, H., Watanabe, T., Morita, S., Otsuka, R., Sugioka,
739 H., Baba, T., Araki, E., & Suyehiro, K. (2006). New discoveries in dynamics of an M8
740 earthquake-phenomena and their implications from the 2003 Tokachi-oki earthquake
741 using a long term monitoring cabled observatory. Tectonophysics, 426(1–2), 95–105.
742 https://doi.org/10.1016/j.tecto.2006.02.021
743 Mulder, T., & Cochonnat, P. (1996). Classification of Offshore Mass Movements. SEPM
744 Journal of Sedimentary Research, Vol. 66. https://doi.org/10.1306/D42682AC-2B26-
745 11D7-8648000102C1865D
746 Mulder, T., Syvitski, J. P. M., Migeon, S., Faugères, J.-C., & Savoye, B. (2003). Marine
747 hyperpycnal flows: initiation, behavior and related deposits. A review. Marine and
748 Petroleum Geology, 20(6–8), 861–882. https://doi.org/10.1016/j.marpetgeo.2003.01.003
749 Nakajima, T., & Kanai, Y. (2000). Sedimentary features of seismoturbidites triggered by the
750 1983 and older historical earthquakes in the eastern margin of the Japan Sea.
751 Sedimentary Geology, 135(1–4), 1–19. https://doi.org/10.1016/S0037-0738(00)00059-2
752 Normandeau, A., Bourgault, D., Neumeier, U., Lajeunesse, P., St-Onge, G., Gostiaux, L., &
753 Chavanne, C. (2020). Storm-induced turbidity currents on a sediment-starved shelf:
754 Insight from direct monitoring and repeat seabed mapping of upslope migrating
755 bedforms. Sedimentology, 67(2), 1045–1068. https://doi.org/10.1111/sed.12673
756 Okal, E. A., & Synolakis, C. E. (2001). Comment on “Origin of the 17 July 1998 Papua New
757 Guinea Tsunami: Earthquake or Landslide?” by E. L. Geist. Seismological Research
758 Letters, 72(3), 362–366. https://doi.org/10.1785/gssrl.72.3.362
759 Özeren, M. S., Çağatay, M. N., Postacioğlu, N., Şengör, a. M. C., Görür, N., & Eriş, K.
760 (2010). Mathematical modelling of a potential tsunami associated with a late glacial
761 submarine landslide in the Sea of Marmara. Geo-Marine Letters, 30, 523–539.
762 https://doi.org/10.1007/s00367-010-0191-1
763 Parker, G. (1982). Conditions for the ignition of catastrophically erosive turbidity currents.
764 Marine Geology, 46(3–4), 307–327. https://doi.org/10.1016/0025-3227(82)90086-X
765 Piper, D. J. W., & Normark, W. R. (2009). Processes That Initiate Turbidity Currents and
766 Their Influence on Turbidites: A Marine Geology Perspective. Journal of Sedimentary
767 Research, 79(6), 347–362. https://doi.org/10.2110/jsr.2009.046

768 Piper, D. J. W., Cochonat, P., & Morrison, M. L. (1999). The sequence of events around the
769 epicentre of the 1929 Grand Banks earthquake: initiation of debris flows and turbidity
770 current inferred from sidescan sonar. Sedimentology, 46(1), 79–97.
771 https://doi.org/10.1046/j.1365-3091.1999.00204.x
772 Polonia, A., Vaiani, S. C., & De Lange, G. J. (2016). Did the A.D. 365 Crete
773 earthquake/tsunami trigger synchronous giant turbidity currents in the Mediterranean
774 Sea? Geology, 44(3), 191–194. https://doi.org/10.1130/G37486.1
775 Pope, E. L., Talling, P. J., & Carter, L. (2017). Which earthquakes trigger damaging
776 submarine mass movements: Insights from a global record of submarine cable breaks?
777 Marine Geology, 384, 131–146. https://doi.org/10.1016/j.margeo.2016.01.009
778 Şengör, A. M. C., Grall, C., İmren, C., Le Pichon, X., Görür, N., Henry, P., Karabulut, H., &
779 Siyako, M. (2014). The geometry of the North Anatolian transform fault in the Sea of
780 Marmara and its temporal evolution: implications for the development of intracontinental
781 transform faults. Canadian Journal of Earth Sciences, 51(3), 222–242.
782 https://doi.org/10.1139/cjes-2013-0160
783 Synolakis, C. E., Bardet, J.-P., Borrero, J. C., Davies, H. L., Okal, E. A., Silver, E. A., Sweet,
784 S., & Tappin, D. R. (2002). The slump origin of the 1998 Papua New Guinea Tsunami.
785 Proceedings of the Royal Society of London. Series A: Mathematical, Physical and
786 Engineering Sciences, 458(2020), 763–789. https://doi.org/10.1098/rspa.2001.0915
787 Xu, J. P., Noble, M. A., & Rosenfeld, L. K. (2004). In-situ measurements of velocity structure
788 within turbidity currents. Geophysical Research Letters, 31(9).
789 https://doi.org/10.1029/2004GL019718
790 Xu, J. P., Swarzenski, P. W., Noble, M., & Li, A.-C. (2010). Event-driven sediment flux in
791 Hueneme and Mugu submarine canyons, southern California. Marine Geology, 269(1–
792 2), 74–88. https://doi.org/10.1016/j.margeo.2009.12.007
793 Yakupoğlu, N., Uçarkuş, G., Kadir Eriş, K., Henry, P., & Namık Çağatay, M. (2019).
794 Sedimentological and geochemical evidence for seismoturbidite generation in the
795 Kumburgaz Basin, Sea of Marmara: Implications for earthquake recurrence along the
796 Central High Segment of the North Anatolian Fault. Sedimentary Geology, 380, 31–44.
797 https://doi.org/10.1016/j.sedgeo.2018.11.002
798 Zitter, T. A. C., Grall, C., Henry, P., Özeren, M. S., Çağatay, M. N., Şengör, A. M. C.,
799 Gasperini, L., de Lépinay, B. M., & Géli, L. (2012). Distribution, morphology and triggers
800 of submarine mass wasting in the Sea of Marmara. Marine Geology, 329–331, 58–74.
801 https://doi.org/10.1016/j.margeo.2012.09.002